Investigating the Effect of Iceberg Aspect Ratio on Submarine Melting

Eric William Hester

May 10, 2018

Abstract

Icebergs play many roles in the dynamics of polar climates. Their geographical, and geometric, distributions have important consequences for shipping, polar ecosystems, and ice sheet-ocean modelling. However, current parameterizations of iceberg deterioration largely ignore their geometry. We examine the influence of aspect ratio and ambient relative velocity on iceberg melting in a series of novel experiments. We find that aspect ratio is an important control on iceberg melting, with lateral melt rates typically exceeding basal melt rates. The standard parameterizations of Weeks and Campbell [37] and the Jenkins three equation model [16] could not reproduce this geometry dependent melting, and underestimate the melt rate. We emphasise that further investigation into the influence of geometry on melting is necessary.

1 An introduction to icebergs

Icebergs are generated by calving at the margins of ice shelves and glaciers, and constitute a large component of the freshwater output from ice sheets, making up 45% of Antarctic freshwater loss [27].

The most obvious impact of icebergs is on shipping. In the aftermath of the sinking of the Titanic, the International Ice Patrol was set up to monitor iceberg locations in the North Atlantic [29]. With projected increases in Arctic shipping, it is crucial to understand the expected distributions of icebergs. Icebergs also have important impacts on ecosystems; nutrient release during melting can boost biological productivity in an area up to 10 times their actual size [33], while bed scouring can have devastating effects on seabed biology [8]. At the largest scales, icebergs can be a dominant component of the freshwater flux from land ice to the ocean in the Greenland and Antarctic ice shelves [11, 23, 31]. As such, understanding their subsequent evolution is key to modelling the interaction between ice sheets and the ocean.

A central factor in modelling icebergs is their size, which determines iceberg evolution and geographical distribution [31]. Many studies have examined iceberg size distribution, in both Greenland [5, 35] and Antarctica [2, 9, 34, 36]. Enormous variation in sizes are observed, from the smallest growlers at several meters wide, to iceberg B-15, the largest iceberg ever recorded, at 300 km $\times$ 40 km. Importantly, there is a large range of iceberg aspect ratios observed in nature, where the aspect ratio is defined as the ratio of iceberg length L to submerged iceberg depth H. Yet there has been very little investigation on the impact of aspect ratio on iceberg melting – typically being ignored in melting parameterizations.

The current treatment of aspect ratio focusses on its impact on iceberg stability [4, 38]. Below a certain length L to total depth D ratio, the iceberg becomes unstable, overturning when

$$\frac{L}{D} < \sqrt{0.92 + \frac{58.32\,\mathrm{m}}{D}}.$$

1.1 Our investigation

The goal of this summer project is to investigate specifically the effect of aspect ratio on iceberg melting in a series of novel laboratory experiments.

We compare our experimental results with two common melting parameterizations, and suggest directions for future investigation, with the ultimate goal to develop improved parameterizations of iceberg deterioration which take into account their geometry and aspect ratio.

2 Models of iceberg melt

The problem of modelling ice melting has been seriously considered for well over one and a half centuries. The formalisation of the moving boundary interface condition was first established by Josef Stefan in his 1889 paper (as cited by [6]).

2.1 Weeks and Campbell 1973 [37]

The first serious attempt to model iceberg deterioration was made by Weeks and Campbell in 1973 [37]. Their goal was to investigate the feasibility of towed icebergs as a fresh water source for arid climates. Surprisingly, they found it was both technologically and economically feasible. In doing so they had to account for the many sources of iceberg deterioration; melting, wave erosion, calving, insolation, and others. We focus on their widely adopted parameterization of iceberg melting.

Weeks and Campbell modelled the melting using empirical relations for turbulent heat transfer over a flat plate [10], resulting from relative motion between the iceberg and water. They saw this motion as a result of towing, but it can arise in nature. Any force other than water drag (air drag, Coriolis force, wave induced motion) will lead to a velocity difference between the ice and water. Furthermore, a sheared water column can result in substantial increases in relative velocities [13]. We now examine Weeks and Campbell's derivation.

The model relies on an empirical relation for the average Nusselt number $\bar{\mathrm{Nu}}$ (a non-dimensional ratio of convective to conductive heat transfer) in turbulent convection [10],

$$\bar{\mathrm{Nu}} = \frac{\bar{h}L}{k},$$

where $\bar{h}$ is the averaged convective heat transfer coefficient, L is a characteristic length, and k is the thermal conductivity of the fluid.

The turbulent heat transfer relation for the Nusselt number in flow past a heated plate is given in term of the non-dimensional Reynolds, Re, and Prandtl, Pr, numbers,

$$\bar{\mathrm{Nu}} = 0.037\,\mathrm{Re}^{0.8}\,\mathrm{Pr}^{1/3},$$

where Re is the ratio of inertial to viscous forces, and Pr is the ratio of heat and momentum transfer,

$$\mathrm{Re} \equiv \frac{UL}{\nu}, \qquad \mathrm{Pr} \equiv \frac{\nu}{\kappa}.$$

Here, $U = |v_i - v_w|$ is the relative velocity between the ice and water, ν is the momentum diffusivity, and κ is the thermal diffusivity, related to the thermal conductivity k by $\kappa = k/\rho_w c_p$, where ρ_w and c_p are the density and heat capacity of seawater.

To determine the melt rate of a given submerged area, A, (either single or multiple faces), we consider the total heat transfer into the ice q, given by

$$q = \bar{h} A \Delta T,$$

where ΔT is the temperature difference between the ice and water. We can then relate the heat absorption of the ice face q to a melt rate u (in units of velocity) through the latent heat Λ

$$u = \frac{q}{A \Lambda \rho_i}.$$

Hence, we recover Weeks and Campbell's relation [37]

$$u = \left(0.037 \frac{\rho_w}{\rho_i} \nu^{-7/15} \kappa^{2/3} \frac{c_w}{\Lambda} \right) \frac{U^{0.8} \Delta T}{L^{0.2}}.$$

It is important to note that this parametrisation implies the melt rate will go to zero as the velocity goes to zero (though turbulence will cease at this point, invalidating the relation).

This issue is addressed by the improved parameterization of FitzMaurice et al. [12]. FitzMaurice et al. found that there are three regimes of iceberg melting, dependent on the behaviour of *meltwater plumes* [12]. These plumes rise along the iceberg sides, driven by the buoyancy of the fresh meltwater. As they rise they become turbulent, entraining the warmer ambient water. Thus, even when the iceberg is stationary relative to the ocean, there is a buoyancy driven flow up the side walls, leading to increased melting. Once the relative velocity of the iceberg becomes comparable to the plume velocity, the upstream plume is detached and swept away. FitzMaurice et al. model this regime by substituting the plume velocity into Weeks and Campbell's parameterization (slightly modified to account for increasing entrainment as the ambient velocity increases, and the appropriate plume temperature). Only at higher velocities, when both the front and rear plumes are detached, is Weeks and Campbell's original parameterization correctly recovered.

2.2 Holland and Jenkins 1999 [16]

A second widely used parameterization of ice melting was derived by Holland and Jenkins [16]. Their parameterization uses the three thermodynamic equations for interfacial temperature T_b and salinity S_b that must be satisfied at the ice-water interface, which in general differ from the far-field values of these quantities, in the ice (T_i, S_i) and water (T_w, S_w).

The temperature at the interface lies on the liquidus line, where the temperature, T_b, is salinity and pressure dependent, and approximated by a linear relation,

$$T_b(S_b) \approx a + bS_b + cp,$$

where p is the pressure and a, b, and c are constants. Heat is conserved at the interface, so that the absorption of latent heat during melting is provided by heat transfer from the ice and water

$$Q^T_{latent} = Q^T_{ice} + Q^T_{water}.$$

A similar relation holds for salinity, though now there is no release of salt during melting of fresh ice, nor any diffusion of salt through the ice.

$$Q^S_{brine} = Q^S_{ice} + Q^S_{water}.$$

Here Q^T_{latent} and Q^S_{brine} are given in terms of the latent heat, Λ, density of ice ρ_i, the melt rate of the ice u, and the interface salinity S_b

$$Q^T_{latent} = -\rho_i u \Lambda, \qquad Q^S_{brine} = -\rho u S_b.$$

The heat flux from the ice is a simple diffusive solution, while the salt flux from the ice is zero. The remaining components, $Q^{T/S}_{water}$, are obtained using a parameterization of turbulent heat and salt transfer. This is the primary development of Holland and Jenkins' work.

In it, the heat and salt transfer are parameterised in terms of transfer coefficients Γ^T and Γ^S, and a drag coefficient C_d

$$Q^{T/S}_{water} = \rho c_p C_d^{1/2} \Gamma^{T/S} U (T_b - T_w),$$

where U is the relative iceberg-ocean velocity. The heat diffusion is modelled by simply using the temperature difference between the ice and interface. Putting these requirements together, the ablation velocity u (and interfacial temperature T_b and salinity S_b) are found by solving the following system of equations

$$\begin{aligned} u(\rho_i \Lambda + \rho_i c_i (T_b - T_i)) &= \rho_w c_w C_d^{1/2} U \Gamma^T (T_w - T_b), \\ u \rho_i S_b &= \rho_w C_d^{1/2} U \Gamma^S (S_w - S_b), \\ T_b &= \lambda_1 S_b + \lambda_2. \end{aligned}$$

However, this parameterization is now completely independent of iceberg geometry, predicting the same melt rate for all sides of an iceberg in uniform ambient flow.

3 Experimental Method

3.1 Measuring a melt rate

We first define a measure of the overall melt rate for an ice block with differing melting between and within each immersed face. There is otherwise no way to compare the melting of different shaped ice blocks. Ideally, we would weight the rate of volume loss by the current submersed surface area, to give a melt rate velocity

$$\frac{1}{A(t)} \frac{dV}{dt}.$$

However as written above it is an instantaneous measure, which is difficult to obtain experimentally. Given that we only have access to the initial and final ice bass values during the experiment, we assume the melt rate velocity u is constant in time, approximating it as

$$u \equiv \frac{2}{A(t) + A(0)} \frac{V(t) - V(0)}{t}.$$

The volume change can be inferred from the mass loss, assuming the density of ice, and the initial area is easily calculated from the dimensions of the block. It is the final area estimation that requires the most effort, and will require several image processing techniques, discussed later.

3.2 Ice preparation

Having defined a metric for the melt rate, we now consider the manufacture of the ice blocks. To minimise bubble formation, fresh water that had been still for at least two days was siphoned into an ice block mold. Unfortunately, a small amount of bubble formation was still observed despite these precautions, though they are not expected to be of relevance. Two mold types were used, with (interior) dimensions $10 \times 15 \times 30$ cm, and $32.5 \times 22.5 \times 6$ cm. These molds were kept in an industrial refrigerator at -30 to -25 °C for one to two days, to allow the entire block to fully freeze and equilibrate to fridge temperature. A wooden handle was frozen into the block using several clamps during the freezing process. The deeper mold was used to generate arbitrary length blocks. This was done by filling up to the desired length, freezing, removing the block, and finally refreezing the handle in the side of now tilted ice block. To visualise the melting of the block, several ml of blue food dye were injected in the water before freezing.

3.3 The experiment

Before each experiment, the mold was removed from the freezer, and dipped in a bucket of room temperature water to release the ice block. Once removed, pictures were taken of the ice using a Nikon Coolpix P7000 camera from approximately 1 m distance. A ruler was included in the picture for distance calibration. The mass of the combined ice and mold was measured before each experiment using a scale with 2 g precision. The temperature of the tank water was measured using a thermometer with 0.1 °C precision before each experiment, and the density at 20.000 °C was measured using an Anton Paar 5000M Density Meter.

The desired immersed depth of the ice block was scored on the side before each experiment, and the block was subsequently immersed in the tank to approximately this depth. Later experiments calibrated the immersed depth by measurement of the dimensions of the handle, iceblock, mold, and tank mount beforehand.

The tank (Fig. 1) was filled with oceanic saltwater of salinity 30 to 31 g/kg, and temperature 18 to 21 °C, which could be pumped through the tank and recirculated at three speeds, 0, 1.5, and 3.5 cm s^{-1}. 40 cm of plastic mesh and a 10 cm honeycomb grating were used to laminarise the incident flow. However, surface tension effects prevented a completely uniform velocity. Instead, the upper surface was stationary, with a roughly 1 cm shear layer below the surface, below which the velocity was approximately uniform. Adding surfactant reduced the pinning, but the effect was only temporary, (and potentially hazardous when reacting with bleach used to suppress algae growth).

The velocities of the tank were previously calibrated using multiple runs of large 'floaters' – polystyrene blocks weighted down by a horizontal plastic cross (of diameter 4 cm and depth 2 cm) located a given distance below the surface. The high drag of the cross forces the floater to move with the average velocity of the fluid at that depth. The time for the floater to traverse 40 cm down the tank was calculated 10 times for each floater, giving the velocity measurement estimate.

The experiments were recorded for 10 minutes using the P7000 camera, after which the blocks were removed from the tank, weighed and photographed from each side to compare the ice shape to the initial dimensions.

3.4 Post-processing

We analyse these post-experiment images to detect the final shape of the iceberg using opencv for Python (Fig. 2). First, the image is cropped to contain only the melted part of the ice block. Then the red channel is used to detec‘ the ice block, as the blue dye absorbs red. A

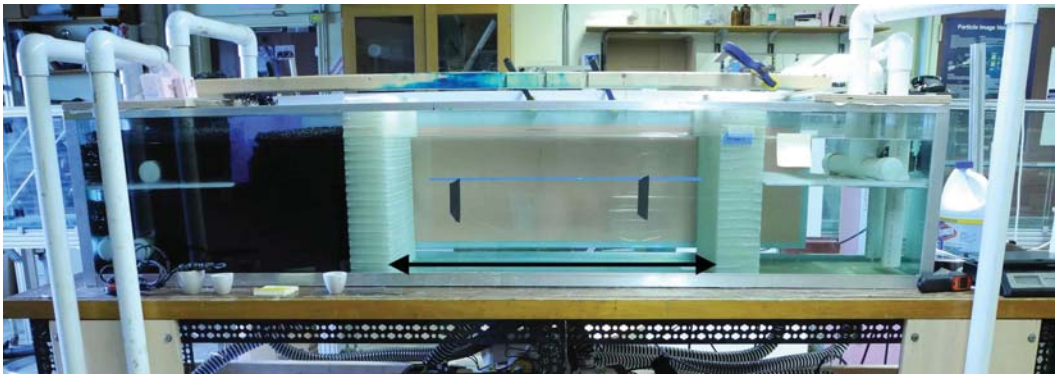

Figure 1: Photo of experimental tank. The central region into which the block is immersed (see black arrow) measures 76.5 cm long, 42 cm wide, and 33.5 cm deep.

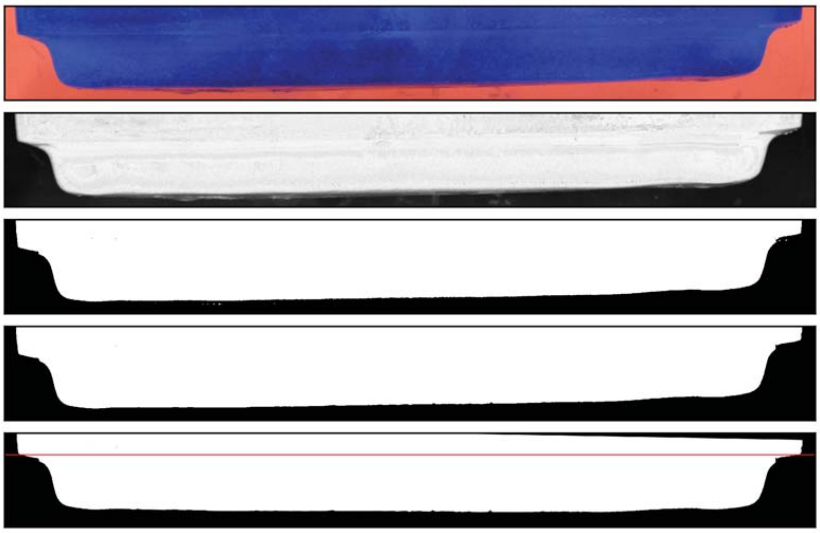

Figure 2: Stages of image processing. The red channel of the image is taken, then a uniform threshold applied to obtain a binary image. An opening morphological transform is used to eliminate noise, followed by corner detection and rotation. The red line is an estimate of the waterline.

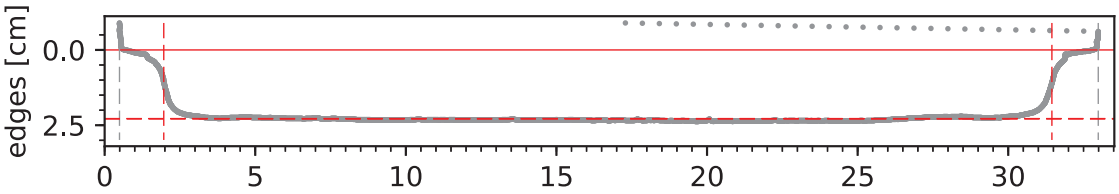

Figure 3: After processing the image, the edges can be detected by looking at leftmost, bottommost, and rightmost white pixels. The initial side edges are shown in dashed gray, the initial bottom edge is the bottom of the graph, and the final shape of the block is given by the solid gray line. The top solid red line is an estimate of the waterline, while the dashed lines are mean values of left, bottom, and right melting.

uniform threshold can then be applied to give a binary image, and inversion applied to give a white block on a black background. This threshold was chosen manually for each image, as different experiments had different lighting conditions. Spurious noise (small numbers of isolated white pixels) is minimised by applying an erosion filter (white pixels near black pixels are switched to black). The resultant shrinking of the ice block pixels is undone by applying a subsequent dilation filter (black pixels adjacent to white are switched to white). This removes small regions of noise, but preserves large features in the image. This process is known as opening the image.

After this process, we detect the left, bottom, and right edges of the image by measuring the leftmost, bottommost, and rightmost white pixels. Using this outline we can then determine final dimensions of the block. To determine the amount of melting we attempted to infer the waterline (the red line in figures 2 and 3). This was the uppermost point at which the ice block had noticeable melting. Specifically, the highest point along the block more than a certain number of pixels to the right/left of the leftmost/rightmost white pixel.

We then estimate an average depth and width from the final ice shape by taking the mean depth between the bottom corners, and the mean width above the highest corner. The distance from the waterline to the mean of the bottom is compared to the initial immersed depth of the ice block to infer a mean basal melt. The side melts are estimated from the difference between the rightmost and leftmost points (of the unmelted portion), and the average right and left sides (Fig. 3).

The conversion ratio of pixel to cm for each photo is assumed to be uniform in each direction, and at each point throughout the image. In reality this is not the case, however several pictures with rulers in both orientations were taken, and differences are typically less than 1 percent.

3.4.1 Experimental video profiles

By subtracting the initial frame from subsequent video frames, and applying thresholding to the result, we estimated side profiles of the ice blocks during the course of the experiment. Example melting profiles for these experiments are shown in figure 6. Unfortunately, the video processing cannot distinguish between the blue of the ice block and the blue of the melt water, leading to poor shape detection for our melting experiments. However, we can discern that the leading edge retreats at a roughly constant rate in time. Owing to these issues the main results use pictures of the final profiles of the ice blocks.

4 Results

Over 50 experiments were performed, with aspect ratios from 0.4 to 13, at three ambient velocities U of 0, 1.5, and 3.5 $\mathrm{cm\,s^{-1}}$. The ambient fluid temperature was kept as constant as possible at around 19 °C ± 2 °C, and the salinity of the water at 30 g/kg.

The main series of experiments examined the influence of aspect ratio using a constant immersed depth of $H = 3\,\mathrm{cm}$, where the streamwise length L varied from 10 cm to 32.5 cm, in approximate increments of 5 cm.

4.1 Qualitative observations

4.1.1 High flow velocity

A time series of two experiments at $U = 3.5\,\mathrm{cm\,s^{-1}}$ is shown in Figure 4, confirming the highly nonuniform nature of ice block melting, both within and between experiments. The frontal melt rate is much larger than that of the base and sides; the incoming flow is at the highest

temperature at the front of the block, and cools as it loses heat into the ice, thereby reducing the melt rate with distance.

The frontal melt is itself also nonuniform with depth, leading to an increasing slope on the leading edge during the experiment. Part of this is expected from the nonuniform velocity profile of the tank mentioned in the methods section, though this is only expected to be a small effect. Further, the fluid speed would increase going toward the bottom edge of the face, as is typical for any flow around a bluff body, enhancing the melt rate.

We also observe a striking non-uniformity in the basal melt, which reaches its maximum *away* from the leading edge. Proceeding downstream along the bottom of the ice, we first see a somewhat turbulent region of increased dye concentration, as implied by our Reynolds number $\mathrm{Re} = UH/\nu \approx 1000$. This increased concentration suggests recirculation, typical of flow separation problems. This pooling of cold meltwater reduces heat replenishment (and hence melting) from the ambient water. Turbulence would still cause some mixing with the ambient water however, entraining heat and mitigating the insulating effect of the region.

Behind this recirculation region, we see a clear maximum in the basal melt. This region moves downstream during the experiment, and has a measurably increased melt rate. Interestingly, the general characteristics of the leading profiles of the two blocks are quite similar, despite their different aspect ratios. The key difference is that the longer ice block extends beyond the local maximum in basal melt, beyond which the melting is lower, and much more uniform. In fact (though difficult to see from the time series in figure 4), the dye pattern has changed from turbulent eddies to steady, straight streaks, suggesting a return to laminar flow after the reattachment region.

This configuration is essentially that of flow past a forward-facing step, which while studied previously [1, 18, 22, 26, 30], has not been thoroughly investigated from the perspective of heat transfer [1, 18]. The general properties of turbulent flow past a forward facing step can be seen in our experiment – flow separation after the leading edge, leading to a region of turbulent recirculation, and subsequent reattachment of the flow. Furthermore, experiments on heat transfer have also found a maximum in the Nusselt number at the point of reattachment [1]. This intuitively makes sense – the fluid at the reattachment point has not been cooled by the ice, so should lead to an increased melt rate. The velocity in this region also has a nonzero component normal to the ice face, which (as with the front face), has been observed to increase the melt rate [21].

Understanding the scaling of this reattachment region is key to predicting whether this local enhancement of the melting observed in the laboratory will be geophysically relevant. A range of values have been found by different authors (summarised in [30]), but for Reynolds

Table 1: Experimental data.

L	Initial Ice block streamwise length	$10, 15, 20, 25, 32.5\,\mathrm{cm}$
W	Initial Ice block transverse width	10–$22.5\,\mathrm{cm}$
H	Initial Ice block immersed depth	3–$20\,\mathrm{cm}$
T_i	Ice block Temperature	-30 to $-4\,^\circ\mathrm{C}$
T_w	Ambient water temperature	18–$21\,^\circ\mathrm{C}$
S_w	Ambient water salinity	30–$31\,\mathrm{g/kg}$
t	Experiment duration	$10\,\mathrm{min}$
U	Ambient water velocity	$0,\ 1.5,\ 3.5\,\mathrm{cm\,s^{-1}}$
ρ_i	Ice density	$0.92\,\mathrm{g/cm^3}$

numbers $\mathrm{Re} = 10^3$ to 10^5, the reattachment length is found to be a small multiple of the step height, ranging from roughly 1 to 5. Our experiments with different relative velocities and iceberg lengths (but identical depths) all reveal a similar location (relative to the leading edge) of the melting region – in agreement with previous studies indicating a depth dependence of the recirculation region length. Should this dependence hold for higher Reynolds numbers (10^7 to 10^9), we can expect the increased melting at the reattachment point to have measurable consequences for real icebergs. If instead the reattachment length is limited to some smaller scale, it may be also related to the scalloping of iceberg undersides (though our experiment did not show evidence of further local maxima in the melting behind the first one).

It is important to note that past experiments of flow past a step [30] wereperformed for two dimensional blocks, in which the step extended the entire length of the channel. In our case (and for that of icebergs), we expect the transverse width to become relevant when it approaches the same order of magnitude as the depth. Indeed, the shorter ice block was also less wide than the longer one (Fig. 4) (10 cm to 22.5 cm). These turbulent reattachment regions were also found on the sides of the ice block, leading to similar regions of increased melt on the transverse sides of the block.

The complex shape evolution of a melting ice block echoes previous investigations on the influence of flow and obstacle geometry on melting [15], dissolution [17], and erosion [24]. Higher velocities will unsurprisingly increase melting, but that melting can be highly nonuniform – emphasising the difficulties of applying current parameterizations to iceberg melting.

The suppressed turbulence observed downstream of the larger block also affects the distribution of meltwater in the water column. The water near the free surface behind the longer ice block is much darker than for the short block, suggesting that a larger proportion of meltwater is reaching the surface – with important consequences for the biological environment surrounding an iceberg, as well as the vertical distribution of the freshwater flux due to iceberg melting.

4.1.2 Low flow velocity

Experiments were also performed for the same dimension ice blocks at the lower velocity of $1.5\,\mathrm{cm\,s^{-1}}$. The same trends can be identified in the $1.5\,\mathrm{cm\,s^{-1}}$ experiments, with a local maximum in the melt rate behind the leading edge, followed by a return to laminar flow, and more uniform lower melt rate, behind this maximum. The length scale of this recirculation region is similar to that observed in the higher velocity experiments.

The main differences are the lower melt rate, and the reduced turbulence of the flow, where the dye streaks appear mostly laminar throughout the experiment. This means meltwater is no longer mixed throughout the depth of the iceberg, and instead pools near the free surface of the water.

4.1.3 Zero flow velocity

The zero velocity experiments unsurprisingly lack any local increases in the melt, unlike the experiments with a relative velocity. However, these experiments also exhibit sinking plumes of dyed water. Though the vast majority of melt water does appear to rise to the surface, these plumes remain unexpected as fresh melt water should be far less dense than ambient salt water, despite the temperature difference. It is believed this stems from the neglect of latent heat in such an assertion. The melting of ice in salt water is a very different process to that of mixing cold fresh water with salt water [14, 19]; during the melting, the latent heat is absorbed from the adjacent salt water. As there is no replenishing of the ambient water from continual circulation, this process can cool the salt water sufficiently that it will sink, entraining the dyed meltwater along with it.

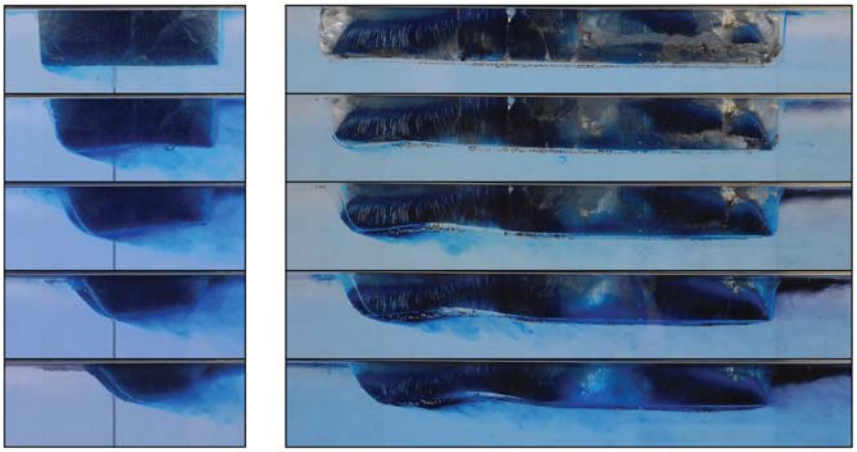

Figure 4: Time series of two experiments with $L = 10$ cm (left) and 32.5 cm (right). Each ice block was immersed up to 3 cm, in ambient water at 20° C, moving at $U = 3.5\,\mathrm{cm\,s^{-1}}$. Frames are shown every two minutes.

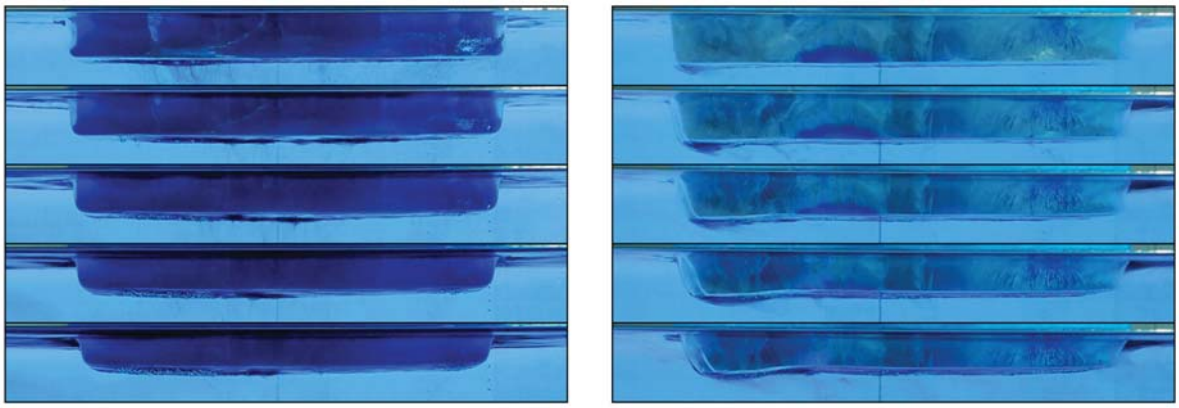

Figure 5: Time series of two experiments with $L = 32.5$ cm (left), for $U = 0$ and $1.5\,\mathrm{cm\,s^{-1}}$ (right).

Figure 6: Measured side profiles of 32.5 cm long ice block immersed in fluid moving at $U = 3.5\,\mathrm{cm\ s^{-1}}$. The edge detection works poorly as a result of the similar colour of the ice block and the dyed melt water. Contours are taken at one minute intervals.

4.2 Quantitative results

4.2.1 Post-experiment picture profiles

Using the image processing techniques described in section 3.4, the final profiles of the melted ice blocks were extracted from the photos taken immediately after each experiment. In figure 7, the average melted profiles of the ice blocks are plotted. The average profile is taken by averaging the profiles from the left and right side of the melted ice block, after aligning at the upstream edge. For each relative fluid velocity, all experimental average melting profiles are plotted on the same graph, revealing broadly similar trends. The profiles are positioned so that the origin corresponds to the location of the front corner of the unmelted ice block. Averaging the left and right profiles is done to compensate for possible asymmetries in the melting and picture processing.

A final melting curve (dashed) was then constructed from the average of the individual experiments. The downstream faces of the ice blocks are omitted from the average calculation, and the most downstream points of the bases for each ice block length are shown with black circles. The grey error bars around the average profile are twice the average of the standard deviations of the individual profiles at each point. The reduced number of profiles at higher lengths affects the standard deviation calculation, but acts as a sensible first estimate of the variability of the melting profiles.

From this averaged profile we can estimate basal and frontal melt. The frontal melt is estimated from the average of the curve between two points identified as the top and bottom of the front face, and average basal melt as the average value of the dashed curve between the start and end of the base. These profiles reveal the disparity between frontal and basal melt for each velocity, highlighting the geometric dependence of iceberg melt (table 2).

As well as the non uniform melting *between* faces, there exist large variations *within* each face. Figure 8 examines the nonuniform basal melt, showing the localised and cumulatively averaged basal melt rate for each of the fluid velocities. Basal melt rates at fluid velocities of $0\,\mathrm{cm\,s^{-1}}$ and $1.5\,\mathrm{cm\,s^{-1}}$ are comparable, though the more turbulent $3.5\,\mathrm{cm\,s^{-1}}$ experiment is markedly increased. This is in agreement with the findings of FitzMaurice et al. [13], who observed a roughly constant melt rate below a threshold fluid velocity – attributed to the influence of rising meltwater plumes. The melt rate was observed to be controlled by the maximum of the velocity of the meltwater plumes and the ambient fluid velocity. FitzMaurice's findings neglected the basal melt however, so her model is not directly applicable to the present experiments.

Instead, the basal melting of our experiments would naturally give rise to a gravity current, as the melt water spreads along the iceberg base to then rise to the surface. The Froude number of gravity currents is approximately unity, and the thickness of the meltwater layer h was observed to be approximately 2 to 4 mm, giving a gravity current velocity of around $\sqrt{gh} \approx 1.4$ to $2.0\,\mathrm{cm\,s^{-1}}$. As such, we expect a weak dependence on the ambient fluid velocity when it is below this gravity current speed. We note however that this is not a confined channel gravity current, and also that some small amount of sinking of the dye was observed. Waves were also observed on the interface which propagated toward the center.

It is worth noting that the average melt rates in table 2 are of the entire dashed lines in figure 7. The average basal melt of a shorter block should be larger, as a larger proportion of the base is in the enhanced melting region. To understand the change in average basal melt with length, we plot the cumulatively averaged basal melt in figure 8. The averaging procedure will naturally reduce the influence of localised features, but we still see a noticeable variation in the average basal melt rate for fluid velocity $3.5\,\mathrm{cm\,s^{-1}}$ as a function of length. This variation in basal melt with length is less pronounced than that between the average frontal and basal melt, and would likely be a secondary effect in the real world, though it is still detectable, with

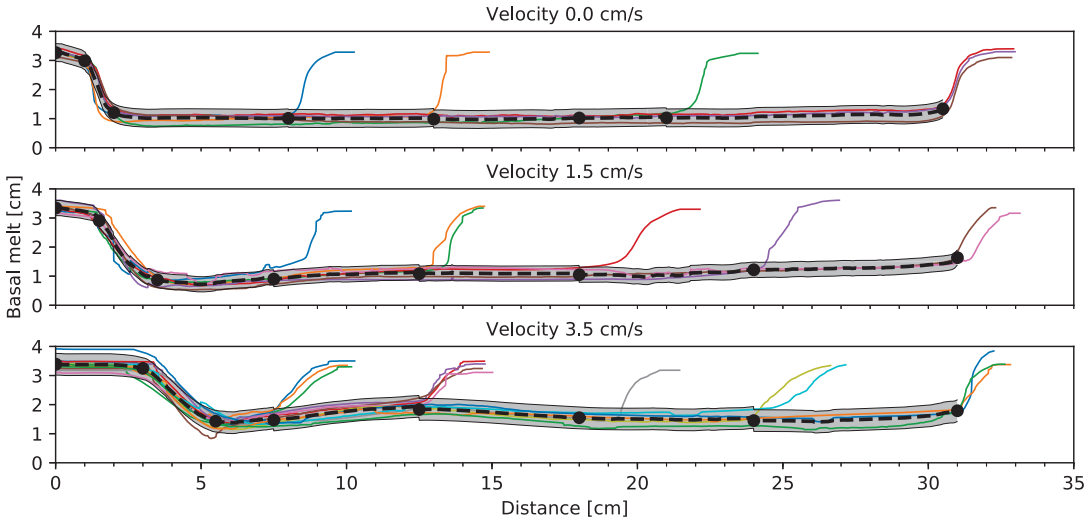

Figure 7: Final profiles of experiments. The profiles are aligned at t heir edge. We observe highly nonuniform melting between and within each face of the block.

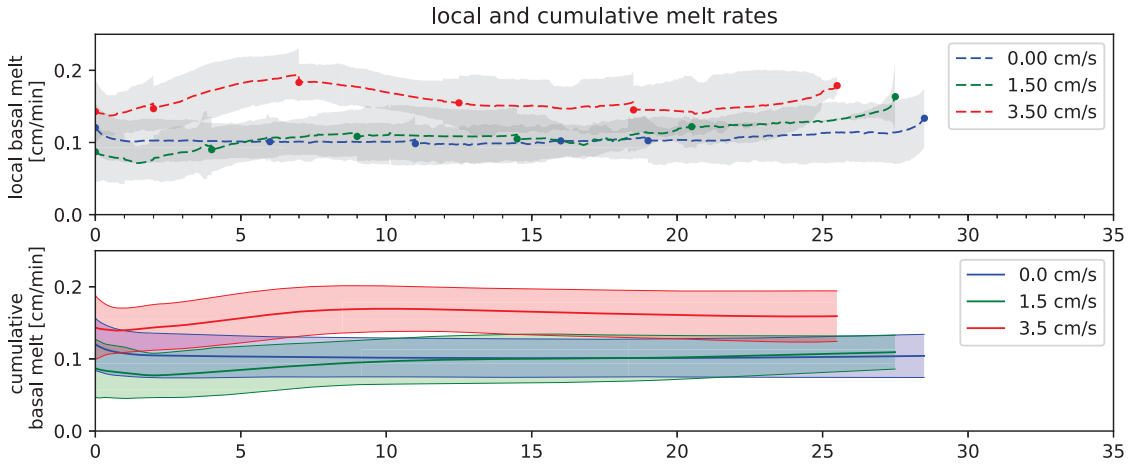

Figure 8: Local and cumulative basal melt rates at 0 cm s^{-1} (blue), 1.5 cm s^{-1} (green), and 3.5 cm s^{-1} (red).

Table 2: Table of average melting rates (cm min^{-1}) of each face.

Face	$U = 0\,\mathrm{cm\,s^{-1}}$	$U = 1.5\,\mathrm{cm\,s^{-1}}$	$U = 3.5\,\mathrm{cm\,s^{-1}}$
Front	0.15 ± 0.03	0.23 ± 0.05	0.41 ± 0.06
Sides	0.13 ± 0.02	0.14 ± 0.03	0.19 ± 0.06
Rear	0.15 ± 0.05	0.13 ± 0.10	0.15 ± 0.11
Base	0.09 ± 0.04	0.10 ± 0.04	0.15 ± 0.04

up to 20% variation in the cumulative basal melt rate.

Figure 8 shows that the $1.5\,\mathrm{cm\,s^{-1}}$ velocity experiments have a slightly increasing basal melt rate with length. This is unfortunately a result of imperfect methodology in deriving melt rates from the final ice block photos. The top corners of the ice blocks, where the melting begins, are actually located somewhat above the water line of the tank. This is thought to result from a positive meniscus forming at the air-water interface on the ice block. The typical amount of above water melting was estimated as 3 mm, however this varied between velocities, experiments, and faces (for $1.5\,\mathrm{cm\,s^{-1}}$). This can be exacerbated by tilting of the ice block when placed in the water. During the freezing process, the wooden handle would sometimes rotate and tilt in the ice, leading to a slight rotation when placed in the tank.

To assess the accuracy of our averaged profile, we also compare it with an automated procedure for calculating the dimensions of individual profile in figure 9, in which the width is calculated from the average of the middle third horizontal section of the block, and the depth is the average of the lowest third of the block. We see broad agreement between the automated calculations, and the dimensions of the averaged profile, with the spread of values typically lying within the uncertainty bars of the averaged melt rate. And again, we see a large difference between typical melt rates observed for each face of the ice block; for non-zero fluid velocity, frontal melting can be two to three times larger than that of the other faces. The basal melt is observed to always be lower than side melting – implying that tabular icebergs with large aspect ratios should melt at a lower rate than smaller aspect ratio icebergs. We additionally observe a slight decrease in the basal melt rate as a function of length at the highest velocities, in accord with the cumulative melt rate calculations discussed earlier.

As a test of our method, we compare estimates of volume loss obtained from the final profiles, and the averaged profile, to the actual volume loss measured from the change in mass over the experiment (Fig. 10). The estimates of volume loss assume that the melting of each face occurs while maintaining a constant rectangular shape, at the rates estimated by the respective method. The uncertainties of the volume loss are half the range of volume losses calculated using upper and lower estimates for each the melt rates of each face. Albeit with some scatter, we see clear agreement between the estimates and direct measurements of volume loss.

Next, we use these estimates of melting to determine an overall melt rate for each experiment (from section 3.1) in figure 11. The volume loss is measured from the change in mass, and the average area inferred using the melt rate estimates from the averaged profiles in table 2, assuming a rectangular shape is conserved during the melt. We note that an additional set of experiments is also used in figures 10 and 11, in which the ice block depth was varied from 5 cm to 20 cm, in increments of 5 cm. We compare our experimental measurements to typically used parameterizations of Weeks and Campbell [37], and the three equation parameterization of Holland and Jenkins [16] (with parameters used in table 3).

We observe a strong decrease in the overall melt rate as aspect ratio is increased, almost halving from tall icebergs (aspect ratio less than unity), to the largest icebergs used (aspect ratio 13). This variation is primarily due to the different relative side areas of each aspect ratio. A longer ice block has a much larger basal area compared to a tall block of the same total area. As such, the overall melting tends to the lower basal melt rate. Shorter blocks are instead more affected by their side melt.

This geometric dependence in the melt is completely absent in the Jenkins' three equation parameterization, and only weakly accounted for in Weeks and Campbell parameterization, each of which underestimate the melting for the parameters used in table 3. This failure stresses the need to account for different side melt rates and side areas in iceberg modelling.

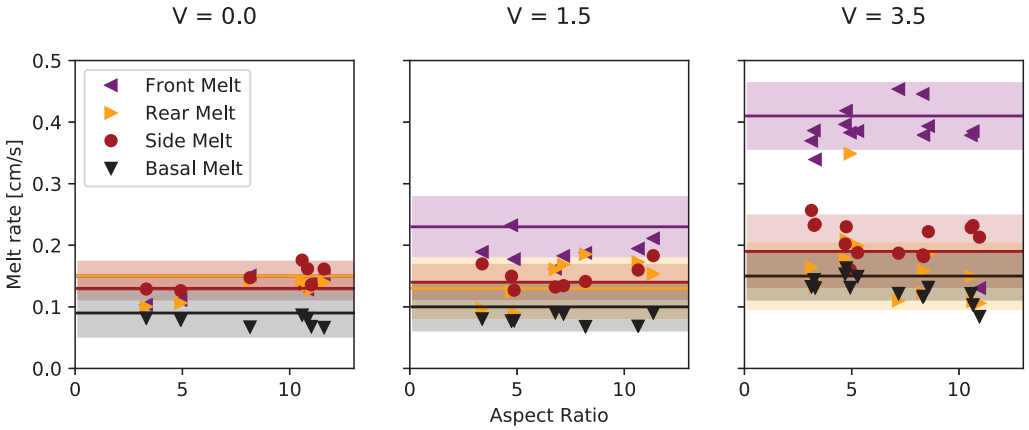

Figure 9: Individual automated side melt calculations (points) and the estimates from the averaged profiles (coloured bars) as a function of aspect ratio. We see agreement between individual and averaged calculations, and strong differences between melt rates on each face of the block.

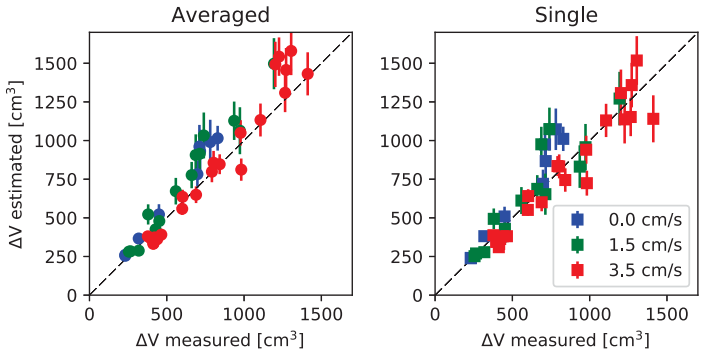

Figure 10: Comparisons of estimated volume loss to measured volume loss, using average (left) and individual (right) profiles, assuming uniform melt on each face (but still varying melt rates between faces). This plot includes additional experiments with greater depths. Uncertainties are estimated as half the range of volumes using high and low estimates for the melt rates.

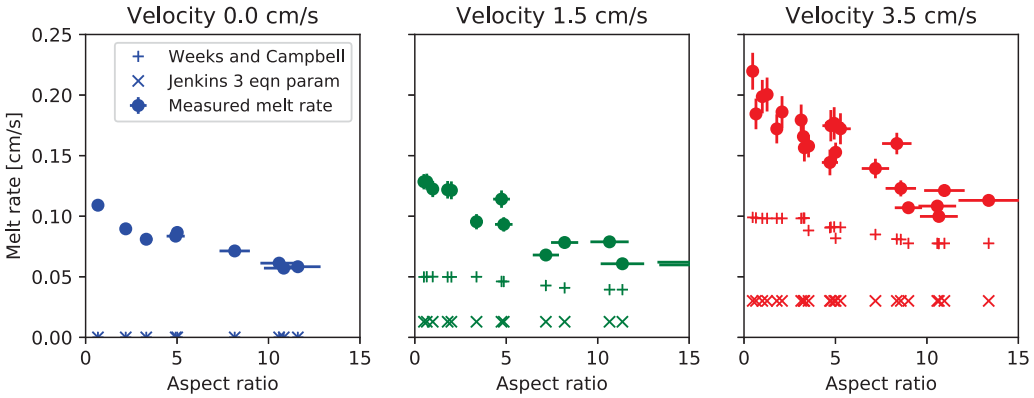

Figure 11: Averaged melt rates of different velocity experiments, as function of aspect ratio, for all sets of experiments. Both the Weeks and Campbell (+) and Jenkins three equation (×) parameterizations are also shown for comparison, using values from table 3. Neither parameterization fully captures the geometric dependence of the ice block melting.

Table 3: Table of values of physical constants, from [3], and [20].

Symbol	Name	Value
T_i	Ice temperature	$-4\,^{\circ}\mathrm{C}$
T_w	Water temperature	$19\,^{\circ}\mathrm{C}$
S_w	Water salinity	$30.5\,\mathrm{g\,kg^{-1}}$
ρ_w	Water density	$1021\,\mathrm{kg\,m^{-3}}$
ρ_i	Ice density	$920\,\mathrm{kg\,m^{-3}}$
ν	Water momentum diffusivity	$1.304 \times 10^{-6}\,\mathrm{m^2\,s^{-1}}$
κ	Water thermal diffusivity	$1.38 \times 10^{-7}\,\mathrm{m^2\,s^{-1}}$
c_w	Water heat capacity	$4192\,\mathrm{J\,kg^{-1}\,^{\circ}C^{-1}}$
c_i	Ice heat capacity	$2108\,\mathrm{J\,kg^{-1}\,^{\circ}C^{-1}}$
Λ	Ice Latent heat	$3.34 \times 10^{5}\,\mathrm{J\,kg^{-1}}$
λ_1	Liquidus slope	$-0.057\,^{\circ}\mathrm{C\,kg\,g^{-1}}$
λ_2	Liquidus intercept	$0.083\,^{\circ}\mathrm{C}$
C_d	Drag coefficient	0.0025
Γ_T	Temperature transfer coefficient	0.011
Γ_S	Salinity transfer coefficient	3.1×10^{-4}

5 Conclusion

Typical existing parameterizations of iceberg melting ignore the possible influence of the iceberg's aspect ratio [16, 37]. To test these models, we ran a series of laboratory experiments, examining the dependence of the melt rate on iceberg size and shape for three different ambient relative velocities. We find that iceberg geometry has a strong effect on the melt rate of icebergs.

Melt rates are highest on the upstream facing side (with respect to the ambient flow), followed by the remaining lateral sides, with lowest melting occurring at the base of the iceberg. Changing the relative area of each face will thus change the overall melt rate.

Furthermore, the melt rate of each face is itself non uniform, with localised regions of increased melt rate of over 50% observed. These regions are believed to correspond to the reattachment zones of separated flow around the ice block [1]. The extent of these regions have been observed to scale with the obstacle height [30], and as such may be geophysically relevant.

To improve melting estimates, we emphasise that melt rates must depend both on the aspect ratio and orientation of the iceberg, in addition to the fluid velocity used by current parameterizations.

6 Acknowledgements

I firstly wish to thank my supervisors Claudia Cenedese and Craig McConnochie for their help throughout this project, whose many thoughts and advice I am deeply grateful for. I greatly appreciate the expertise and help provided by Anders Jensen in building (and fixing) the experimental apparatus. I also thank my fellow GFD scholars for vastly improving an already excellent experience with your friendship, humour, and support. Finally, to all other GFD staff members and visiting guests, I have truly enjoyed my experience of the culture of inquiry (and fun) you have fostered over the years. I will always remember this summer fondly and look forward to meeting many of you in the future.

References

1. Abu-Mulaweh, H. Turbulent mixed convection flow over a forward-facing step—the effect of step heights. *International Journal of Thermal Sciences* **44,** 155–162 (2005).
2. Andres, M., Silvano, A., Straneo, F. & Watts, D. R. Icebergs and Sea Ice Detected with Inverted Echo Sounders. *Journal of Atmospheric and Oceanic Technology* **32,** 1042–1057 (2015).
3. Batchelor, G. *An Introduction to Fluid Dynamics* (Cambridge University Press, 2000).
4. Bigg, G. R., Wadley, M. R., Stevens, D. P. & Johnson, J. A. Modelling the dynamics and thermodynamics of icebergs. *Cold Regions Science and Technology* **26,** 113–135 (1997).
5. Budd, W. F., Jacka, T. H. & Morgan, V. I. Antarctic Iceberg Melt Rates Derived from Size Distributions and Movement Rates. *Annals of Glaciology* **1,** 103-112 (1980).
6. Crepeau, J. Josef Stefan: His life and legacy in the thermal sciences. *Experimental Thermal and Fluid Science* **31,** 795–803 (2007).
7. Dinniman, M. S., Asay-Davis, X. S., Galton-Fenzi, B. K., Holland, P. R., Jenkins, A. & Timmermann, R. Modeling Ice Shelf/Ocean Interaction in Antarctica: A Review. *Oceanography* **29,** 144–153 (2016).
8. Dowdeswell, J. & Bamber, J. Keel depths of modern Antarctic icebergs and implications for sea-floor scouring in the geological record. *Marine Geology* **243,** 120–131 (2007).
9. Dowdeswell, J. A., Whittington, R. J. & Hodgkins, R. The sizes, frequencies, and freeboards of East Greenland icebergs observed using ship radar and sextant. *Journal of Geophysical Research: Oceans* **97,** 3515–3528 (1992).
10. Eckert, E. & Drake, R. *Heat and Mass Transfer* (R.E. Krieger Publishing Company, 1959).
11. Enderlin, E. M., Hamilton, G. S., Straneo, F. & Sutherland, D. A. Iceberg meltwater fluxes dominate the freshwater budget in Greenland's iceberg-congested glacial fjords. *Geophysical Research Letters* **43.** 2016GL070718, 11, 287–11, 294 (2016).
12. FitzMaurice, A., Cenedese, C. & Straneo, F. Nonlinear response of iceberg side melting to ocean currents. *Geophysical Research Letters* **44.** 2017GL073585, 5637–5644 (2017).
13. FitzMaurice, A., Straneo, F., Cenedese, C. & Andres, M. Effect of a sheared flow on iceberg motion and melting. *Geophysical Research Letters* **43.** 2016GL071602, 12, 520–12, 527 (2016).

14. Gade, H. G. Melting of Ice in Sea Water: A Primitive Model with Application to the Antarctic Ice Shelf and Icebergs. *Journal of Physical Oceanography* **9,** 189–198 (1979).

15. Hao, Y. L. & Tao, Y.-X. Heat Transfer Characteristics of Melting Ice Spheres Under Forced and Mixed Convection. *Journal of Heat Transfer* **124,** 891–903 (Sept. 2002).

16. Holland, D. M. & Jenkins, A. Modeling Thermodynamic Ice–Ocean Interactions at the Base of an Ice Shelf. *Journal of Physical Oceanography* **29,** 1787–1800 (1999).

17. Huang, J. M., Moore, M. N. J. & Ristroph, L. Shape dynamics and scaling laws for a body dissolving in fluid flow. *Journal of Fluid Mechanics* **765** (2015).

18. Jayakumar, J. S., Kumar, I. & Eswaran, V. Hybrid mesh finite volume CFD code for studying heat transfer in a forward-facing step. *Physica Scripta* **2010,** 014060 (2010).

19. Jenkins, A. The Impact of Melting Ice on Ocean Waters. *Journal of Physical Oceanography* **29,** 2370–2381 (1999).

20. Jenkins, A., Nicholls, K. W. & Corr, H. F. J. Observation and Parameterization of Ablation at the Base of Ronne Ice Shelf, Antarctica. *Journal of Physical Oceanography* **40,** 2298–2312 (2010).

21. Josberger, E. G. & Martin, S. A laboratory and theoretical study of the boundary layer adjacent to a vertical melting ice wall in salt water. *Journal of Fluid Mechanics* **111,** 439–473 (1981).

22. Largeau, J. F. & Moriniere, V. Wall pressure fluctuations and topology in separated flows over a forward-facing step. *Experiments in Fluids* **42,** 21 (Nov. 2006).

23. Martin, T. & Adcroft, A. Parameterizing the fresh-water flux from land ice to ocean with interactive icebergs in a coupled climate model. *Ocean Modelling* **34,** 111–124 (2010).

24. Moore, M. N. J., Ristroph, L., Childress, S., Zhang, J. & Shelley, M. J. Self-similar evolution of a body eroding in a fluid flow. *Physics of Fluids* **25,** 116602 (2013).

25. Neshyba, S. & Josberger, E. G. On the Estimation of Antarctic Iceberg Melt Rate. *Journal of Physical Oceanography* **10,** 1681–1685 (1980).

26. Pearson, D. S., Goulart, P. J. & Ganapathisubramani, B. Investigation of turbulent separation in a forward-facing step flow. *Journal of Physics: Conference Series* **318,** 022031 (2011).

27. Rignot, E., Jacobs, S., Mouginot, J. & Scheuchl, B. Ice-Shelf Melting Around Antarctica. *Science* **341,** 266–270 (2013).

28. Russell-Head, D. S. The Melting of Free-Drifting Icebergs. *Annals of Glaciology* **1,** 119 122 (1980).

29. Savage, S. in *Geomorphological Fluid Mechanics* (eds Balmforth, N. J. & Provenzale, A.) 279–318 (Springer Berlin Heidelberg, Berlin, Heidelberg, 2001).

30. Sherry, M. J., Jacono, D. L., Sheridan, J., Mathis, R. & Marusic, I. Flow separation characterisation of a forward facing step immersed in a turbulent boundary layer.

Sixth International Symposium on Turbulence and Shear Flow Phenomena, 1325 (2009).

31. Silva, T. A. M., Bigg, G. R. & Nicholls, K. W. Contribution of giant icebergs to the Southern Ocean freshwater flux. *Journal of Geophysical Research: Oceans* **111.** C03004, n/a–n/a (2006).
32. Smith, F. T. Laminar flow of an incompressible fluid past a bluff body: the separation, reattachment, eddy properties and drag. *Journal of Fluid Mechanics* **92,** 171–205 (1979).
33. Smith, K. L., Robison, B. H., Helly, J. J., Kaufmann, R. S., Ruhl, H. A., Shaw, T. J., Twining, B. S. & Vernet, M. Free-Drifting Icebergs: Hot Spots of Chemical and Biological Enrichment in the Weddell Sea. *Science* **317,** 478–482 (2007).
34. El-Tahan, M., Venkatesh, S. & El-Tahan, H. Validation and Quantitative Assessment of the Deterioration Mechanisms of Arctic Icebergs. *Journal of Offshore Mechanics and Arctic Engineering* **109,** 102–108 (Feb. 1987).
35. Tournadre, J., Bouhier, N., Girard-Ardhuin, F. & Remy, F. Large icebergs characteristics from altimeter waveforms analysis. *Journal of Geophysical Research: Oceans* **120,** 1954–1974 (2015).
36. Venkatesh, S. & El-Tahan, M. Iceberg life expectancies in the Grand Banks and Labrador Sea. *Cold Regions Science and Technology* **15,** 1–11 (1988).
37. Weeks, W. F. & Campbell, W. J. Icebergs as a Fresh-Water Source: An Appraisal. *Journal of Glaciology* **12,** 207-233 (1973).
38. Weeks, W. & Mellor, M. Some elements of iceberg technology. English (1978).